A Free-Standing Boron-Doped Diamond Grid Electrode for Fundamental Spectroelectrochemistry

Hannah K. Patenaude, Nastasija Damjanovic, Jason Rakos, Dustyn C. Weber, Aaron I. Jacobs, Samuel A. Bryan, Amanda M. Lines, William R. Heineman, Shirmir D. Branch, and Cory A. Rusinek*

ABSTRACT: Spectroelectrochemistry (SEC) is a powerful technique that enables a variety of redox properties to be studied, including formal potential (E^o), thermodynamic values (ΔG, ΔH, ΔS), diffusion coefficient (D), electron transfer stoichiometry (n), and others. SEC requires an electrode which light can pass through while maintaining sufficient electrical conductivity. This has been traditionally composed of metal or metal oxide films atop transparent substrates like glass, quartz, or metallic mesh. Robust electrode materials like boron-doped diamond (BDD) could help expand the environments in which SEC can be performed, but most designs are limited to thin films (~100−200 nm) on transparent substrates less resilient than free-standing BDD. This work presents a free-standing BDD grid electrode (G-BDD) for fundamental SEC measurements, using the well-characterized $Fe(CN)_6^{3-/4-}$ redox couple as proof-of-concept. With a combination of cyclic voltammetry (CV), thin-layer SEC, and chronoabsorptometry, several of the redox properties mentioned above were calculated and compared. For $E^{o\prime}$, n, and D, similar results were obtained when comparing the CV [$E^{o\prime}$ = +0.279 (±0.002) V vs Ag/AgCl; n = 0.97; $D = 4.1 \times 10^{-6}$ cm^2·s^{-1}] and SEC [$E^{o\prime}$ = +0.278 (±0.001) V vs Ag/AgCl; n = 0.91; $D = 5.2 \times 10^{-6}$ cm^2·s^{-1}] techniques. Both values align with what has been previously reported. To calculate D from the SEC data, modification of the classical equation used in chronoabsorptometry was required to accommodate the G-BDD electrode geometry. Overall, this work expands on the applicability of SEC techniques and BDD as a versatile electrode material.

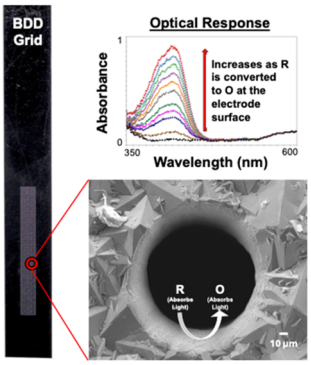

INTRODUCTION

Understanding redox properties is of broad interest to fundamental and applied research inside and outside the chemistry community. While several electrochemical methods are available to characterize redox couples, spectroelectrochemistry (SEC) offers several advantages, including increased sensitivity and selectivity.[1] SEC is frequently performed by combining an electrochemical technique with a spectroscopic method like UV−visible spectrophotometry (UV−vis) or spectrofluorometry, but several other optical detection modes have been reported (Infrared, Raman, X-ray, etc.).[2−4] For SEC with UV−vis, observed absorbance changes occur proportionally to the applied potential and can be used to determine parameters like formal potential ($E^{o\prime}$), thermodynamic values (ΔG_{cell}, ΔH, ΔS), diffusion coefficient (D), and electron transfer stoichiometry (n) for a given redox reaction. Common OTEs include metal mesh designs from materials like Pt or Au, or transparent, conductive films like indium tin oxide (ITO) or boron-doped diamond (BDD) on a transparent substrate.[5−7]

BDD has many favorable features as an electrode material, including low background current, wide potential window, rapid electron transfer kinetics, and excellent mechanical rigidity.[8−13] Applications of BDD electrodes span wastewater treatment,[14,15] inorganic trace metal determination,[12,16] neurochemical analyses,[17−19] and measurements in harsh environments.[19−23] Given the opacity due to the boron-doping, BDD OTEs are typically either in the form of thin films on substrates like quartz or as a coating on a metal mesh (i.e., Nb, Ta) that contain small, macroscale holes.[1] However, because the films are thin, they can lack some of the robust features of BDD needed to survive harsh environments. Additionally, literature on the use of free-standing BDD for SEC is limited with only recent reports from the Macpherson group.[24,25] Overall, there are few options for resilient BDD OTEs capable of withstanding harsh environments like strong acids and bases or high-temperature molten salts.

In this work, we present a free-standing BDD grid electrode (G-BDD) design for SEC measurements. The G-BDD electrode is made of 0.375 mm thick polycrystalline diamond with no underlying substrate. BDD material of this sort has been characterized by the Einaga and Macpherson groups.[26,27] Laser cutting was used to fabricate the grid for optical measurements. As a proof of concept, the model 1-electron

transfer ferri/ferrocyanide ($Fe(CN)_6^{3-/4-}$) redox couple was studied, in addition to the UV−vis absorbance change from colorless to yellow when oxidizing Fe(II) to Fe(III). $E^{o\prime}$, D, n, and the heterogeneous electron transfer rate constant (k) were calculated using cyclic voltammetry (CV) for general electrode characterization. The G-BDD electrode was compared to an identical BDD electrode without the laser-cut grid ("nongrid": NG-BDD). The resulting $E^{o\prime}$, n, and D values were compared for the two electrodes (G-BDD vs NG-BDD) and two techniques (SEC vs CV). This work supports a novel grid electrode designed with resilient, high-performing material to advance fundamental redox chemistry in a variety of media.

EXPERIMENTAL SECTION

Chemicals and Materials. Potassium nitrate (KNO_3), potassium chloride (KCl), potassium ferricyanide ($K_3Fe(CN)_6$), and potassium ferrocyanide trihydrate ($K_4Fe(CN)_6 \cdot 3H_2O$) were purchased from Sigma-Aldrich. Sulfuric acid (H_2SO_4, trace-metal grade), sodium hydroxide (NaOH), and phosphate buffered saline (PBS) were purchased from VWR. Ultrapure water (18.2 MΩ-cm) was used for all standard solutions using a D2798 Barnstead water purification system. Silver−silver chloride (Ag/AgCl, 3.5 M KCl) miniature reference electrodes were purchased from eDAQ and were used for SEC measurements. Ag/AgCl (3.0 M KCl) reference electrodes purchased from BASi, Inc. and used for all CV studies. A 1 mm platinum (Pt) wire (99.95%) from Strem Chemicals was used as the counter electrode for all measurements except the potential window studies where a graphite counter electrode was used.

Instrumentation. Optical and electrochemical measurements were completed in a homemade 1 × 1 cm cuvette, except for the potential window studies which were performed in a 25 mL electrochemical cell. For the SEC studies, the Ag/AgCl reference and Pt counter electrodes were fixated in the corners of the cuvette out of the light path. The working electrode (grid) was positioned in the center of the cuvette in the region of the light path; Figure 1 shows a schematic. All

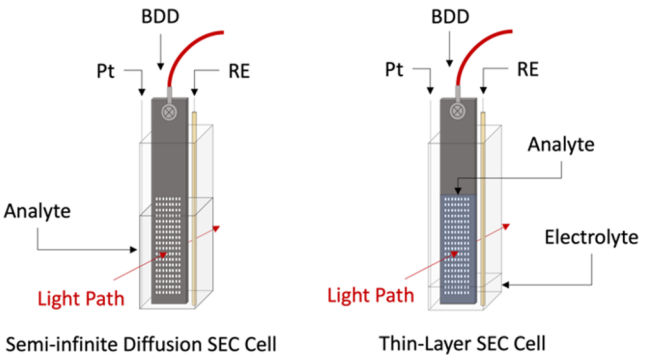

Figure 1. SEC cells with BDD OTE for semi-infinite (left) and thin-layer (right) diffusion experiments.

electrochemical measurements were completed using either a SP-300 (Biologic, USA) or a PalmSens EmStat3+ (BASi, Inc.). For the optical measurements, a DH-2000 BAL light source and HR4000 spectrometer from Ocean Insight were used. For the control study, an Agilent Cary 100 UV−vis spectrophotometer was used. A JEOL JSM-5600 scanning electron microscope was used for imaging.

The (i) grown side, (ii) nucleation side, (iii) native cross-section, and (iv) laser-cut cross-section of a G-BDD electrode were analyzed with Raman spectroscopy using an inVia confocal Raman microscope (Renishaw, Wotton-under-Edge,-Glouchestershire, U.K.). The instrument was attached to a continuous wave, diode-pumped solid-state laser (100 mW max. with 1 mW applied at the sample) using a 532 nm excitation wavelength focused with a 50× objective lens. Spectra were collected at room temperature from 2000 to 200 cm^{-1} with a 10 s integration time for 10 accumulations. Cross-sectional measurements of a G-BDD were made by fracturing the BDD electrode and collecting the Raman spectra at native and laser-cut BDD. The four regions sampled, and the line scan direction are diagrammed in Figure 3C.

BDD Grid Electrode. Electrochemical processing (EP) grade free-standing BDD with custom dimensions was purchased from Elementsix (Santa Clara, CA). This material has been previously characterized by the Macpherson Group and a CVD diamond handbook is available from Element-six.[26−28] Similar FS-BDD from Elementsix can be purchased for ∼$140/$cm^2$ at the time of this publication, so the cost is reasonable.[29] USD Diamond Technology Innovations (Olympia, WA) completed the laser-cutting process (laser spot size: 50 μm). The dimensions of the BDD grid electrodes were 9 mm (wide) × 45 mm (long) × 0.375 mm (thick). A 3 mm diameter hole was cut at the top-center of the material for electrical connection to be made using a ring terminal. The grid was cut into the lower portion of the material in the form of 120 rows and 10 columns of holes. Each hole was laser-cut to 100 μm in diameter with a spacing of 150 μm (edge-to-edge).

Prior to the completion of any electrochemical experiments, all BDD electrodes were cleaned following the procedure outlined by the Macpherson Group.[30−35] The electrodes were placed in H_2SO_4, heated to boiling, and KNO_3 was added to saturation. The cleaned electrodes were first sonicated in deionized water, followed by sonication in ultrapure isopropanol.

To determine $E^{o\prime}$, a thin layer (TL) electrode was constructed using strips of 0.170 mm thick polyethylene film (McMaster-Carr) placed on both sides of the BDD (grown and nucleation) along the long edges of the grid (left and right). Then, cut-to-size microscope slides were positioned on each side of the electrode and fixed using a quick-cure epoxy. A side-on view of the TL electrode is shown in Figure S1. The analyte solution was then added into the "spacer" region and held through capillary action. Finally, a small amount of 1.0 M KCl was placed at the bottom of the cuvette to create an ionic connection to the Ag/AgCl reference (eDAQ) and Pt counter electrodes that were affixed to corners of the cuvette with the quick-cure epoxy.

Chronoabsorptometry was performed in a similar cell to determine D, but the diffusion layer was not restricted. In this case, the cuvette was filled with the analyte solution and the grid area was fully submerged. Schematics of both the TL and semi-infinite diffusion (SID) cell setup are shown in Figure 1. In both setups, the irradiation diameter for the fiber optics was 600 μm and the path length of the cuvette was 1 cm.

RESULTS AND DISCUSSION

Material Characterization. The BDD grids were first characterized using scanning electron microscopy (SEM). SEM micrographs in Figure 2A,B show the "grown side" of the

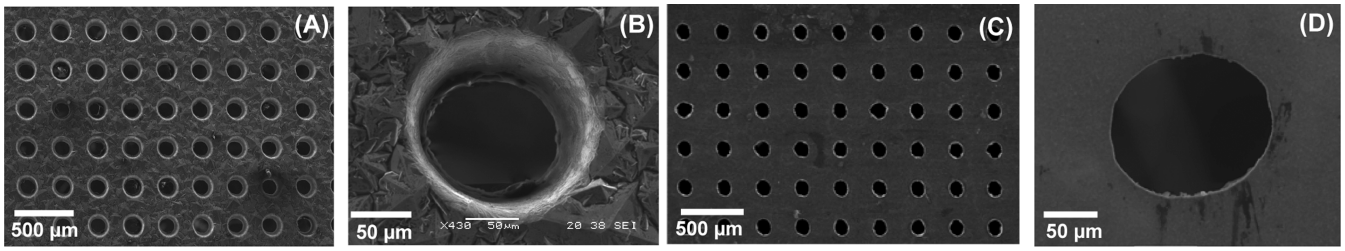

Figure 2. SEM of the grown (A and B) and nucleation (C and D) sides of the BDD Grid.

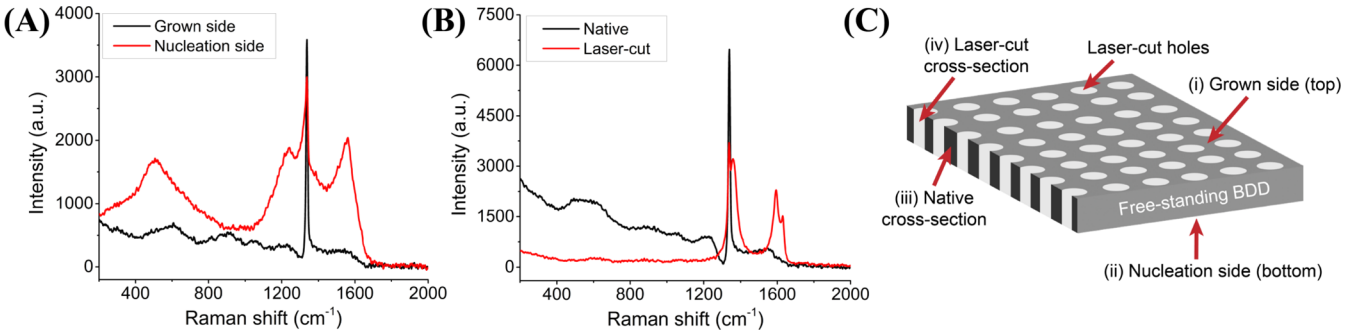

Figure 3. Raman spectra of G-BDD electrodes. (A) Spectral comparison of the grown vs nucleation side; (B) Spectral comparison of the cross section. (C) Schematic of the G-BDD electrode depicting the regions analyzed.

BDD material, while Figure 2C,D show the "nucleation side." The nucleation side of free-standing BDD was initially attached to a tungsten (W) substrate which was etched away after the chemical vapor deposition (CVD) growth process. Due to the diamond seeding process that was used to deposit BDD onto the substrate, the crystal grain size is expected to be much smaller for the nucleation side than the grown side. This is evident when comparing Figure 2B (grown side) and Figure 2D (nucleation side). The crystallites appear on the order of 10−20 μm on the grown side, while submicron crystallinity was observed on the nucleation side. The laser-cutting process was performed with the grown side facing the laser, and as a result Figure 2B,D indicate that there may be a taper in the cut from the grown side to the nucleation side considering the hole diameter in Figure 2B is approximately 15−20 μm larger than that shown in Figure 2D. Based on Figure 2A,C, it also appears that the holes on the grown side present greater symmetry than those on the nucleation side.

The G-BDD electrodes' boron concentration was determined using secondary-ion mass spectroscopy (SIMS) measurements completed at Eurofins, USA. The measurement was focused on a region near the top and away from the grid. A boron concentration of 3.0×10^{20} atoms·cm^{-3} was obtained, as shown by the SIMS depth profile in Figure S2. The reported value is based on an average of the flat region of the depth profile and is indicative of a "high" boron-doping level.[8] Higher or lower doping levels may be desirable for specific applications and could be adjusted accordingly in the CVD process.

Representative Raman spectra of the G-BDD electrode are presented in Figure 3. The spectrum of the grown side (Figure 3A, black) shows an intense, sharp peak at 1336 cm^{-1}. This is attributed to the zone-center optical phonon of diamond. The asymmetric shape of the optical phonon peak is caused by Fano resonance which is observed in semimetallic BDD with boron doping levels $\sim\geq 10^{20}$ B atoms cm^{-3}.[36] The BDD electrodes presented in this work have a doping concentration of $\sim 3 \times 10^{20}$ atoms cm^{-3} based on the SIMS profile in Figure S2. The presence of Fano resonance and the B levels determined by SIMS are both consistent with semimetallic BDD. Weakly intense, broad peaks occur at ca. 600 and 1220 cm^{-1} on the grown side. These are associated with the presence of B in polycrystalline diamond. The intensity of these peaks relative to the zone-center optical phonon is further evidence of B-doping levels sufficient to produce a semimetallic BDD.[36−38] Lastly, a weakly intense, broad G-band peak appears around 1565 cm^{-1}, which results from scattering by sp^2 nondiamond carbon (NDC). Based on the low intensity, the grown side contains little sp^2 NDC. The spectrum of the nucleation side (Figure 3A, red) shows distinct differences from the grown side. The zone-center optical phonon is still observed at 1336 cm^{-1} but is more asymmetrical. Additionally, the peak at 600 cm^{-1} is red-shifted to 510 cm^{-1} and both the 510 and 1220 cm^{-1} peaks are more intense. These changes are evidence of higher boron doping levels at the nucleation side.[38] Lastly, a broad G-band signal at 1565 cm^{-1} is about 7-times more intense on the nucleation side than the grown side, indicating that sp^2 NDC features are more abundant.

Next, a G-BDD electrode was fractured to expose cross sections of the native BDD and the laser-cut holes. A schematic of the regions investigated is provided in Figure 3C. Representative Raman spectra of these two regions are presented in Figure 3B at a depth of 180 μm. The spectrum of the native cross section (Figure 3B, black) is similar to the grown side in Figure 3A, with the zone-center optical phonon of diamond at 1336 cm^{-1}, B-related peaks at 600 and 1220 cm^{-1}, and a sp^2 NDC G-band at 1595 cm^{-1}. The B-doping level in the G-BDD cross-section is higher than at the surface of the grown side as evidenced by more intense peaks at 600 and 1220 cm^{-1} and increased Fano resonance. The G-band is slightly more intense in the native BDD cross-section compared to the grown side, which reflects a higher sp^2 NDC content. After laser cutting the BDD, there was a

Table 1. Figures of Merit Determined from G-BDD and NG-BDD for $Fe(CN)_6^{3-/4-}$ in 1.0 M KCl[a]

electrode	pre-treatment?	technique	$E^{o\prime}$ (3.5 M C1$^-$) (V)	$E_{pa} - E_{pa}/2$ (V)	n	ΔE_p* (V)	D_R (cm^2/s)	k (cm/s)
G-BDD	yes	CV	+0.279	0.058	0.97	0.064	4.1×10^{-6}	1.4×10^{-2}
G-BDD	no	CV	+0.281	0.074	0.76	0.112	5.4×10^{-6}	1.6×10^{-3}
NG-BDD	yes	CV	+0.282	0.058	0.97	0.067	5.1×10^{-6}	1.2×10^{-2}
NG-BDD	no	CV	+0.283	0.067	0.84	0.096	2.9×10^{-6}	1.8×10^{-3}
G-BDD	yes	SEC	+0.278		0.91		5.2×10^{-6}	

[a]Constant of 6 used in G-BDD SEC chronoabsorptometry equation to calculate D. *For 0.05 V/s scan rate. For determination of k with pretreated G-BDD, only scans with $\Delta E_p \geq 63$ mV were used.

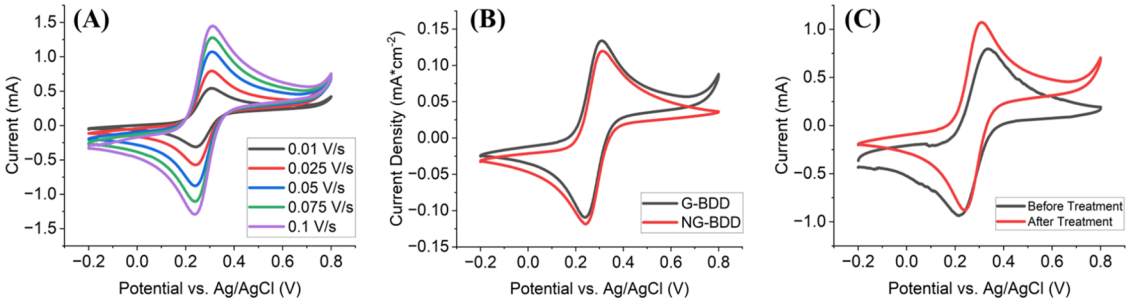

Figure 4. Cyclic voltammograms of 1.0 mM $Fe(CN)_6^{3-/4-}$ in 1.0 M KCl using G-BDD and NG-BDD. (A) Scan rate study using G-BDD from 0.01 to 0.1 V/s, (B) overlay of CVs with G-BDD and NG-BDD after anodic treatment at 0.05 V/s, and (C) overlay of CVs with G-BDD before and after anodic treatment at 0.05 V/s. Reference electrode: Ag/AgCl. Counter electrode: Pt.

significant increase in G-band intensity. This is expected since laser cutting is known to induce sp^2 NDC in BDD.[32] Two intense peaks emerged at 1360 and 1630 cm^{-1}. These are attributed to the D- and D′-disorder bands of amorphous sp^2 NDC, respectively.[39,40] The presence of G- and D-bands indicates that there is both ordered and dislocated sp^2 NDC in the lattice. Therefore, the laser cutting seems to create a mixture of graphite-like sp^2-hybridized NDC and sp^3-hybridized polycrystalline diamond on the inner surface of the laser-cut holes.[41] Since Raman spectra are produced by subsurface features, this lattice structure must extend a depth into the material surrounding the hole walls.[42] The cross-sectional spectra remained relatively constant across the depth profile of both the native and laser-cut cross sections (Figure S3).

Electrochemical Characterization. Cyclic voltammetry (CV) was used to assess the electrochemical performance of the G-BDD electrodes. Results were compared to an identical BDD electrode with no grid (NG-BDD). This was completed to observe changes in the electrochemical response brought about by the presence of residual nondiamond carbon due to the laser-cutting process. After acid cleaning the electrodes, an anodic pretreatment in 1.0 M H_2SO_4 using CV was also performed where the potential was scanned from +2.5 to −1.5 V at 0.1 V/s for 30 cycles. It is important to note that previous studies including such pretreatment on laser-cut BDD reported pH-dependent quinone groups on the sp^2-rich laser-cut BDD areas, but they are not expected to impact spectroelectrochemical studies.[32−34]

CVs were recorded on both electrodes in 1 mM $Fe(CN)_6^{4-}$ in 1.0 M KCl before and after pretreatment. Several redox parameters were determined and are given in Table 1. A series of CVs were recorded at varied scan rates (0.01−0.1 V·s^{-1}) within a potential window of −0.2 to +0.8 V. Each scan rate was cycled three times and repeated for three trials. The geometric surface area of the electrode submerged in solution was 6.61 cm^2 for NG-BDD and 8.01 cm^2 for G-BDD. iR compensation was completed prior to all measurements using the current interrupt method (1 or 10 mA, 50 ms current pulses).[43] The uncompensated resistance was automatically accounted for (80% compensation) using the EC-Lab Software (Biologic, LLC, USA). The method outlined by Nicholson was used to determine k for any CV measurement with a peak-to-peak (ΔE_p) separation ≥63 mV.[44] For ΔE_p values below 63 mV, determination of k by this method is not quantitative. It is also important to note that the Nicholson method assumes diffusion to a planar electrode. However, while the grown side of the G-BDD electrode exhibits a characteristic roughness, a good approximation of k can still be obtained due to the time scale of the CV experiment. With the scan rates used, the length of the diffusion layer (δ) is larger than the grown-side roughness (R_a) of <50 μm reported by Elementsix for a similar type of EP-grade BDD.[28] For example, for a CV scan from −0.2 to +0.8 V at 0.05 V·s^{-1} using $\delta = (Dt)^{1/2}$ ($D = 5 \times 10^{-6}$ cm^2·s^{-1}), δ is ∼100 μm.

As seen in Table 1, the values for $E^{o\prime}$ were similar across all four electrodes, ranging from +0.279 ± 0.002 V to +0.283 ± 0.001 V vs Ag/AgCl, which agree with values reported for the $Fe(CN)_6^{3-/4-}$ couple on BDD.[45] The CV i−E curves from the scan rate study on G-BDD after pretreatment are shown in Figure 4A. Using the Randles-Sevcik equation below, a plot of i_p vs $v^{1/2}$ yielded a linear response on all electrodes, indicative of semi-infinite linear diffusion.

$$i_p = 2.69 \times 10^5 n^{3/2} A D^{1/2} C v^{1/2} \quad (1)$$

All values obtained for D ranged on the expected order of magnitude (10^{-6} cm^2·s^{-1}). Values of 4.1 and 5.4 × 10^{-6} were obtained on pretreated G- and NG-BDD, respectively, and both align with literature.[46] The untreated electrodes slightly underestimated D, and this is likely due to the higher degree of irreversibility relative to the treated electrodes (ΔE_p—Table 1).

Figure 4B,C show CV overlays for the pretreated G-BDD vs pretreated NG-BDD (Figure 4B) and the pretreated vs

untreated G-BDD (Figure 4C). Figure 4B shows a close overlay in the response between the pretreated G- and NG-BDD electrodes. The slight increase in the anodic response at +0.8 V is the beginning of the surface sp^2-carbon peak observed in the KCl background (Figure S4E, discussed below). There is a visual difference in the pretreated vs untreated G-BDD in Figure 4C. Overall, $E_p - E_{p/2}$ was lower on the pretreated electrodes than the untreated BDD: 0.058 V was observed on both G- and NG-BDD, with 0.074 and 0.067 V from their untreated counterparts. ΔE_p followed a similar trend. These results correspond to larger k values on the treated electrodes; pretreated G-BDD was over an order of magnitude larger than the untreated material, as seen in Table 1. This may suggest the presence of quinone groups on the surface due to sp^2-hybridized carbon at the laser-cut regions of the BDD grid as a result of the pretreatment process, which has been reported on previously.[32] In general, these results confirm that the pretreatment process results in an improved response toward $Fe(CN)_6^{3/4-}$ and that the electrochemical activity is not hindered by the laser-cutting of the grid.

Using the pretreated electrodes, the potential window for both BDD electrodes was then examined in five aqueous electrolytes: 1.0 M H_2SO_4, 1.0 M NaOH, 1.0 M phosphate-buffered saline (PBS), 1.0 M KNO_3, and 1.0 M KCl. The results are shown in Figure 5 for the G-BDD and NG-BDD

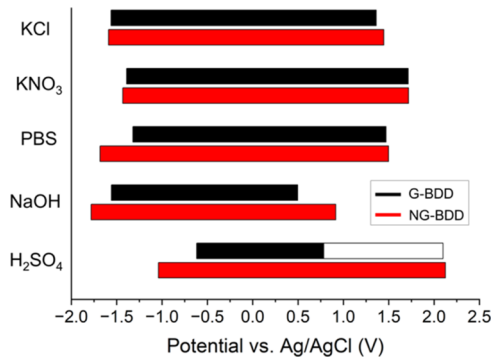

Figure 5. Potential windows in different media on BDD with and without the laser-cut grid at 0.05 V/s. Reference electrode: Ag/AgCl (3.5 M KCl) with a double junction for corresponding electrolyte. Counter electrode: graphite.

electrodes in each electrolyte, and the respective CV i–E curves are shown in Figure S4A–E. A threshold of 0.4 mA·cm^{-2} was used in the oxygen- and hydrogen-overpotential regions to determine the anodic and cathodic potential window, as previously described by the Macpherson group.[32] In PBS, KNO_3, and KCl, the potential window was generally similar on both BDD electrode types. The following magnitudes were observed: PBS −3.18 V (NG-BDD) and 2.79 V (G-BDD); KNO_3 −3.15 V (NG-BDD) and 3.10 V (G-BDD); and KCl −3.04 V (NG-BDD) and 2.92 V (G-BDD). These values agree with previous findings.[30−35,45−52] In KNO_3, an anodic peak ca. +1.2 V was observed on both electrodes, but with a larger magnitude on G-BDD (1.34 vs 1.22 mA·cm^{-2}). This peak has been attributed to signatures of sp^2-carbon, so the increased signal on G-BDD is expected.[32]

With G-BDD in 1.0 M H_2SO_4, prominence of the oxygen reduction reaction (ORR) at cathodic potentials and oxidation of surface sp^2-carbon at anodic potentials caused a decrease in the potential window compared to NG-BDD. This is evident in Figure S4A and as a result, the potential window was found to be 1.42 V. With baseline correction, however, this nearly doubles to 2.85 V. 3.16 V was observed with NG-BDD with no baseline correction needed.

Measurements completed in 1.0 M NaOH (Figure S4B) also yielded a difference between the potential window of the BDD electrodes. A potential window of 2.70 V was observed on NG-BDD, while 2.05 V was observed on G-BDD. The oxygen-overpotential (OH^- oxidation) accounted for most of the difference in the potential window (NG-BDD: 0.92 V, G-BDD: 0.50 V), again, likely due to the presence of sp^2-hybridized carbon.[13,53−56] This effect of nondiamond carbon appears to be exacerbated with 1.0 M NaOH compared to the other electrolytes, signifying that G-BDD is more sensitive to OH^- oxidation. Overall, while the laser-cutting process reduces the potential window for G-BDD, it is not to the degree that the electrode performance would be hindered in any of the electrolytes studied.

Spectroelectrochemical Characterization. The $Fe(CN)_6^{3-/4-}$ redox couple was used again since the reduced form (ferrocyanide) does not absorb light in the visible region and the oxidized form (ferricyanide) exhibits strong absorption at 420 nm (ε = 1020 M^{-1}·cm^{-1}). Two SEC techniques were used: thin-layer (TL) and semi-infinite diffusion (SID). The TL measurements yield $E^{o\prime}$ via a Nernst plot (log([O]/[R]) vs E_{cell}). This regression combines the Nernst equation and the Beer–Lambert law, summarized via the equation below.[57,58]

$$E_{cell} = E^{o'} + \frac{2.303RT}{nF}\log\left(\frac{[O]}{[R]}\right)$$

$$\frac{[O]}{[R]} = \frac{\frac{Abs_2 - Abs_1}{\varepsilon b}}{\frac{Abs_3 - Abs_2}{\varepsilon b}} = \frac{Abs_2 - Abs_1}{Abs_3 - Abs_2} \quad (2)$$

Abs_1 represents the absorbance value when the analyte is fully reduced (no $E_{applied}$), Abs_2 represents the absorbance value at a given magnitude of $E_{applied}$, and Abs_3 represents the absorbance value when the analyte is fully oxidized. More information can be found in Kissinger and Heineman on pgs. 68–77.[57] For both the TL and SID studies, the analyte began as the colorless $Fe(CN)_6^{4-}$ and oxidizing potentials were applied to generate the yellow $Fe(CN)_6^{3-}$ solution. Results for the TL and SID experiments are shown in Figures 6 and 7, respectively.

The UV–vis spectra obtained for the TL study are shown in Figure 6A, showcasing the expected characteristic peak shape for $Fe(CN)_6^{3-}$, with a λ_{max} ca. 420 nm. In this experiment, the potential was stepped from 0 to +0.4 V vs Ag/AgCl in increments of 0.05 V after +0.15 V. The potential was held at each step for 5–8 min until the absorbance and current stabilized. As the potential was increased, a proportional increase in the absorbance response was observed, indicating the conversion of Fe(II) to Fe(III) in the TL cell. Using the absorbance value at λ_{max} (420 nm), a Nernst plot was generated and is shown in Figure 6B, exhibiting excellent linearity (R^2 = 0.999). Since the y-intercept of the Nernst plot yields $E^{o\prime}$, this value was determined to be +0.278 (±0.001) V vs Ag/AgCl (3.5 M KCl).

After normalizing the Ag/AgCl reference potential with a Cl^- concentration of 3.5 M for all electrodes, $E^{o\prime}$ by TL-SEC is nearly identical in magnitude to all other measurements completed with CV (Table 1). No statistical difference in $E^{o\prime}$

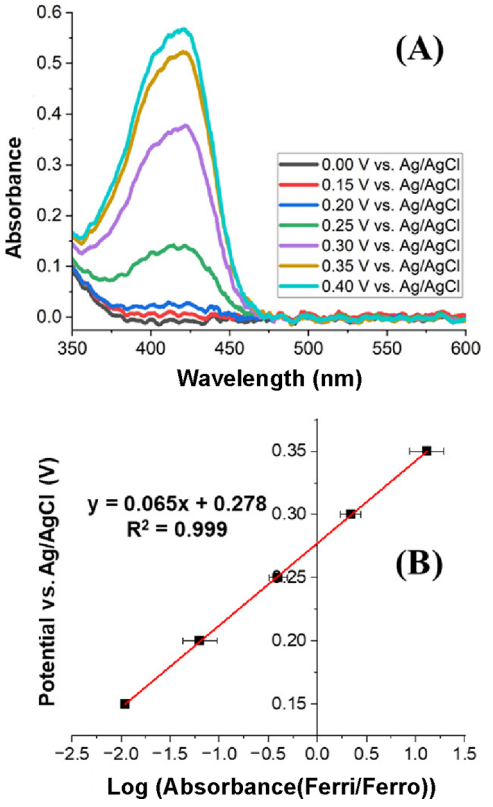

Figure 6. Thin-layer SEC of 25 mM $Fe(CN)_6^{3-/4-}$ in 1.0 M KCl using the G-BDD OTE. (A) UV−vis absorbance spectra as a function of applied potential. (B) Nernst plot used for the calculation of $E^{0\prime}$ and n. Reference electrode: Ag/AgCl. Counter electrode: Pt.

was observed between TL-SEC and CV on G-BDD (95% confidence). The slope of the Nernst plot ($0.059/n$) was used to determine n. The value observed with TL (0.91) was also close to what was obtained using CV with pretreated G-BDD (0.97) and NG-BDD (0.97).

The SID measurements were completed using chronoabsorptometry where a single potential step was applied such that the BDD grid electrode potential was held at 0.0 V vs Ag/AgCl for 20 s before stepping to +0.8 V for 120 s. Based on the combined CV and TL results shown in Figures 4A and 6A, +0.8 V gave sufficient overpotential to keep the process diffusion limited. The absorbance response at 420 nm was then monitored over time before and after the potential step. Five trials were conducted for all measurements and averaged to provide the reported values.

Figure 7A shows Abs vs t at 420 nm for the entirety of the measurement. Figure 7B displays the chronoabsorptometry plot (Abs vs $t^{1/2}$), and the 0-time point is taken as the moment the potential step to +0.8 V vs Ag/AgCl was made. In both figures, there are two regions of separate slope, indicating that G-BDD follows the trend for previous work using mini-grid electrodes.[59] The region after 3 s in Figure 7B (highlighted in red), is attributed to G-BDD exhibiting a pseudoplanar surface (discussed below). A strong linear relationship was obtained in this region (y [absorbance] = 0.0079x [absorbance·$s^{-1/2}$] + 0.048 [absorbance], R^2 = 0.996).

To accurately determine D from this data, the three-dimensional geometry of the G-BDD electrode must be considered. It is different from the equation that has been classically used to define the relationship between absorbance and time after an electrochemical potential step:

$$\text{Abs} = 2\varepsilon_O b D^{1/2} C t^{1/2} \pi^{-1/2} \tag{3}$$

This equation holds for an electrode with one conductive side, where the light path only traverses one diffusion layer on the singular electrode surface (e.g., BDD thin film on one side of a quartz slide). This relationship is derived by combining the Beer−Lambert Law,

$$\text{Abs} = \varepsilon l C \tag{4}$$

with the charge-concentration relationship:

$$Q = nFAC \tag{5}$$

the equation simplifies to

$$\frac{\text{Abs}}{Q} = \frac{\varepsilon l}{nF\text{A}} \tag{6}$$

and can be combined with the Anson equation below.

$$Q = 2nFACD^{1/2} t^{1/2} \pi^{-1/2} \tag{7}$$

All terms have their usual meaning.

However, with multiple conductive sides to the OTE, the light path will include multiple, distinct diffusion layers. This was first postulated by the Murray group in 1971 using an Au grid electrode that was conductive on both sides, and they modified the Abs vs $t^{1/2}$ relationship accordingly:[59]

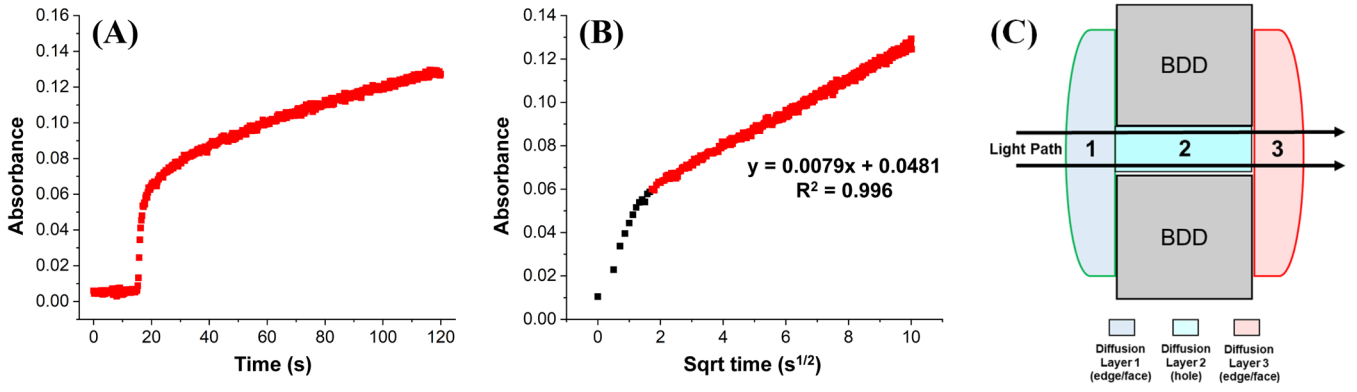

Figure 7. Chronoabsorptometry data for semi-infinite diffusion SEC of 1.0 mM $Fe(CN)_6^{3-/4-}$ in 1.0 M KCl using the G-BDD OTE. (A) Absorbance vs time for entire measurement. (B) Absorbance vs $t^{1/2}$ for the determination of D. Units for slope in red region are absorbance·$s^{-1/2}$.Reference electrode: Ag/AgCl; counter electrode: Pt. (C) Schematic of light path traversing 3 diffusion layers in G-BDD.

$$\text{Abs} = 4\varepsilon_O l D^{1/2} C t^{1/2} \pi^{-1/2} \quad (8)$$

This derivation is similar to the one described above, only now considering that the Beer–Lambert Law must be doubled since a diffusion layer would develop on both sides of the Au OTE (Abs = $2\varepsilon lC$). It is important to note that the thickness of the Au grid electrode was no larger than ~8 μm, which is nearly 50× smaller than G-BDD. The Murray group reported additional theory on SEC with their Au mini-grid electrodes that is applicable to G-BDD. When evaluating the Q vs $t^{1/2}$ response at short time scale, they mentioned that the diffusion layer is small relative to the wire dimension and linear diffusion will prevail.[58] The slope of the plot in this time scale is proportional to the microscopic surface area (A_{mic}). Bard and Faulkner describe A_{mic} as "the surface over all its undulations, crevices, and asperities, even down to the atomic level".[43] At sufficiently long times, the diffusion layer will become large relative to the hole and wire dimensions.[58] This will then cause the diffusion layers from individual wires to merge, linear diffusion will dominate, and the slope of the plot is proportional to the geometric or macroscopic surface area (A_{mac}). The averaged diffusion profile under this condition would cause the grid to behave as a pseudoplanar surface. In turn, the Q vs $t^{1/2}$ response should exhibit separate short- and long-time linear segments and only in the case where $A_{mic} = A_{mac}$ will the slopes be the same.

With the Abs vs $t^{1/2}$ response, Murray et al. mentioned that most of the characteristics would be similar to Q vs $t^{1/2}$. However, only the solution present in or above a hole would interact with the light path and the response from any solution present above an outer wire would be "shadowed" and not optically observed.[58] This means that for linear Abs vs $t^{1/2}$ response, diffusion conditions where the grid exhibits a pseudoplanar surface need to be obtained. Therefore, the electrolysis time needed to obtain the pseudoplanar surface can be estimated by calculating the amount of time it would take to produce a diffusion profile depth one-half of the mini-grid hole size using

$$\frac{C_{(x,t)}}{C^b} = 0.50 = \text{erf}\left(\frac{x}{2D^{1/2}t^{1/2}}\right) \quad (9)$$

where x is the hole diameter size. This could then cause the Abs vs $t^{1/2}$ plot to exhibit two regions of different slope at short and long time scales, depending on the hole size.

The phenomena discussed above would be expected to hold true with G-BDD; however, the thickness of G-BDD (0.375 mm) is 50× larger than any Au mini-grid studied by the Murray group.[58] Therefore, the diffusion layer development inside the 0.1 mm diameter, 0.375 mm deep holes must also be taken into consideration, which is depicted in Figure 7C. Using the equation above, the time needed to reach a pseudoplanar surface with G-BDD is about 3 s, for a theoretical value of 5×10^{-6} cm^2·s^{-1} for D of $Fe(CN)_6^{4-}$. At this time point, the diffusion layer thickness is on the order of 40 μm and walls within the conductive "tubes" confine the electrogenerated $Fe(CN)_6^{3-}$ diffusion direction away from the electrode surface. At a diffusion layer thickness of 40 μm that builds in all directions, a tube diameter of 100 μm (0.1 mm), and a length of 375 μm (0.375 mm), it is reasonable to consider the tube as an additional diffusion region through which the light path traverses, as depicted in Figures 7C and S5. Considering this third diffusion layer would cause an additional modification to the Abs vs $t^{1/2}$ relationship. The Beer–Lambert Law would need to be tripled (Abs = $3\varepsilon lC$) and completing the same derivation as described previously yields

$$\text{Abs} = 6\varepsilon_O l D^{1/2} C t^{1/2} \pi^{-1/2} \quad (10)$$

In the Abs vs $t^{1/2}$ plot (Figure 7B), the time point where the slope magnitude changes is ca. 3 s and is in direct agreement with the value calculated using the formula shown above. After this, G-BDD exhibited a pseudoplanar surface (Figure 7B). This region was then used to determine D for $Fe(CN)_6^{4-}$ using the Abs vs $t^{1/2}$ relationship for 3 diffusion layers and 5.2×10^{-6} cm^2·s^{-1} was obtained. This generally agrees with all other electrodes and methods studied and what has been reported in the literature.[45,46,55]

For justification, if a constant of 4 is used in the Abs vs $t^{1/2}$ relationship, D becomes 1.2×10^{-5} cm^2·s^{-1}, causing a deviation from the other electrodes/methods studied using CV. These results prove that (1) the SID-SEC response with G-BDD follows that published previously for other mini-grid electrodes, and (2) the constant in the chronoabsorptometry equation for G-BDD must be larger than 4 due to its characteristic thickness of 0.375 mm.

SID SEC Control Studies. Three separate control studies were completed: a benchmark with a Pt-mesh electrode, a comparative measurement using two models of UV–vis spectrophotometers, and reversal of the G-BDD direction so that the nucleation-side, rather than the grown-side, of the electrode faced the light path.

With the Pt-mesh electrode, the same SEC cell design as G-BDD was used (25 mM $Fe(CN)_6^{4-}$ in 1 M KCl). A constant of 4 was used for two conductive sides, as suggested previously.[59] A value of 7.3×10^{-6} cm^2·s^{-1} was calculated for D. If a constant of 2 was used, the value inflated to 2.3×10^{-5} cm^2·s^{-1}, far from the expected value. Additionally, a set of measurements was completed with G-BDD using a benchtop UV–vis spectrophotometer (Agilent Cary 100). The SEC cell design was the same as with the Ocean Optics setup used previously and the concentration of $Fe(CN)_6^{4-}$ was 1.0 mM. Using a constant of 6, a value for D of 5.1×10^{-6} cm^2·s^{-1} was determined, nearly identical to the 5.2×10^{-6} cm^2·s^{-1} obtained with Ocean Optics.

Lastly, the G-BDD electrode was flipped so that the nucleation-side of the material faced the light path. Up to this point, all measurements were conducted with the grown-side facing the light path. As seen in Figure 2, the holes in G-BDD were laser-cut from the grown-side to the nucleation-side. A slight taper in the hole was observed as the laser cut through the BDD and the holes on the nucleation-side ranged 10–25 μm smaller in diameter than the grown-side. Considering what this means for the light path exiting a hole smaller in diameter than the entrance hole, diffraction is likely to occur with the light exiting the nucleation-side. It is possible that internal reflection could also occur, but this was unlikely due to the nature of the BDD inside the holes. So, by reversing the G-BDD direction, the light would exit a hole with a wider diameter than it entered, and verification was needed to determine any effect on the response.

The Abs vs $t^{1/2}$ (n = 3) response is shown in Figure S6 (gray-blue) and the shape of the plot is similar to that seen in Figure 7B (black-red). The electrolysis time (gray portion, Figure S6) needed to reach a pseudoplanar surface (blue portion, Figure S6) was nearly identical to the grown-to-nucleation results ca. 3 s. A strong linear correlation was observed in the time frame where the electrode behaved

pseudoplanar (y [Abs] = 0.0074x [Abs·s$^{-1/2}$] + 0.0388 [Abs], R^2 = 0.996). This corresponded to a value for D of 4.59 × 10^{-6} cm^2·s^{-1}, which is directly in-line with that obtained with the other electrodes and measurements reported in Table 1. This indicates that the orientation of the G-BDD electrode with these dimensions does not have a significant impact on the Abs vs $t^{1/2}$ response. In all three cases, the control measurements support modification of the chronoabsorptometry equation to accommodate the G-BDD electrodes and possible development of three diffusion layers.

While we have proposed this modification to the Abs vs $t^{1/2}$ relationship considering three diffusion layers, it is likely that the value for the constant lies somewhere between 4 and 6 and is dependent on several factors. These factors could include the electrode thickness, diameter of the grid holes, and spacing between holes. Such variations were out of the scope of this paper but will be the focus of future work to elucidate the Abs vs $t^{1/2}$ relationship for SEC with electrodes like G-BDD.

CONCLUSIONS

An optically transparent, free-standing BDD grid electrode (G-BDD) was fabricated and characterized topographically, electrochemically, and spectroelectrochemically. Several important redox parameters were calculated using the Fe(CN)$_6^{3-/4-}$ redox couple, such as $E^{o\prime}$, D, n, and k. A pretreatment process was used, and the response was compared before and after. Additionally, BDD electrodes of the same dimensions without the laser-cut grid were used as a control. Good agreement was observed between the calculated redox parameters for both electrodes.

Chronoabsorptometry was also completed to determine D for Fe(CN)$_6^{4-}$ and 5.2 × 10^{-6} cm^2·s^{-1} was obtained. To calculate this value, however, modification of the traditional chronoabsorptometry equation that relates absorbance to $t^{1/2}$ (Abs vs $t^{1/2}$) was required. Due to the characteristic thickness of the G-BDD OTE (0.375 mm), the light path must pass through three different diffusion layers: one on either face (two) and one within the 0.1 mm diameter, 0.375 mm thick grid holes. Decades ago, the Murray group first published on this phenomenon on multiple conductive surfaces of OTEs and the light path traversing multiple diffusion layers. However, they used Au grid electrodes and largely considered them a surface with two distinct diffusion regions (increasing the constant from 2 to 4). The G-BDD OTEs used in this work contain three distinct diffusion regions and, thus, required further modification of the constant (from 4 to 6). The constant is expected to be somewhere between 4 and 6 and dependent on factors like electrode thickness, hole diameter, and hole center-to-center spacing and these features will be a focus of future work. Overall, the work reported here expands the applicability of BDD as an electrode material and spectroelectrochemical techniques as a suitable method for characterizing redox analytes in a range of environments.

ASSOCIATED CONTENT

Supporting Information

The Supporting Information is available free of charge at

Experimental details include chemicals, materials, and instrumentation used throughout the work; SIMS plot is also presented to determine the boron concentration in the BDD grid electrode; the CV i–E responses for the potential window studies are shown as well as the data for the SEC control studies (PDF)

AUTHOR INFORMATION

Corresponding Author

Cory A. Rusinek − *Radiochemistry Program, Department of Chemistry and Biochemistry, University of Nevada, Las Vegas, Las Vegas, Nevada 89154, United States; Department of Chemistry and Biochemistry, Miami University, Oxford, Ohio 45056, United States;* orcid.org/0000-0002-6852-0219; Phone: 01-513-529-2457; Email: rusineca@miamioh.edu

Authors

Hannah K. Patenaude − *Radiochemistry Program, Department of Chemistry and Biochemistry, University of Nevada, Las Vegas, Las Vegas, Nevada 89154, United States; Inorganic, Isotope, and Actinide Chemistry, Los Alamos National Laboratory, Los Alamos, New Mexico 87545, United States;* orcid.org/0000-0002-6790-4659

Nastasija Damjanovic − *Radiochemistry Program, Department of Chemistry and Biochemistry, University of Nevada, Las Vegas, Las Vegas, Nevada 89154, United States*

Jason Rakos − *Radiochemistry Program, Department of Chemistry and Biochemistry, University of Nevada, Las Vegas, Las Vegas, Nevada 89154, United States; Department of Chemistry and Biochemistry, Miami University, Oxford, Ohio 45056, United States; Nuclear and Chemical Engineering, Pacific Northwest National Laboratory, Richland, Washington 99352, United States*

Dustyn C. Weber − *Radiochemistry Program, Department of Chemistry and Biochemistry, University of Nevada, Las Vegas, Las Vegas, Nevada 89154, United States; Department of Chemistry and Biochemistry, Miami University, Oxford, Ohio 45056, United States*

Aaron I. Jacobs − *Department of Chemistry, Michigan State University, East Lansing, Michigan 48823, United States;* orcid.org/0009-0006-5767-522X

Samuel A. Bryan − *Nuclear and Chemical Engineering, Pacific Northwest National Laboratory, Richland, Washington 99352, United States;* orcid.org/0000-0002-8826-0880

Amanda M. Lines − *Nuclear and Chemical Engineering, Pacific Northwest National Laboratory, Richland, Washington 99352, United States*

William R. Heineman − *Department of Chemistry, University of Cincinnati, Cincinnati, Ohio 45221, United States*

Shirmir D. Branch − *Nuclear and Chemical Engineering, Pacific Northwest National Laboratory, Richland, Washington 99352, United States*

Notes

The authors declare no competing financial interest.

ACKNOWLEDGMENTS

This research is being performed using funding from the DOE Office of Nuclear Energy's Nuclear Energy University Program through Project 20-19188 and the University Nuclear Leadership Program Graduate Fellowship. The authors would also like to acknowledge Diamond Technology Innovations, LLC for their assistance in the lasing of the

BDD grid. Vivian Flaum is also acknowledged for helpful discussions. Prof. Greg M. Swain is also acknowledged for help with the Raman measurements.

REFERENCES

(1) Heineman, W. R. *J. Chem. Educ.* **1983**, *60* (4), 305−308.
(2) Živcová, Z. V.; Frank, O.; Petrák, V.; Tarábková, H.; Vacík, J.; Nesládek, M.; Kavan, L. *Electrochim. Acta* **2013**, *87*, 518−525.
(3) Ashley, K.; Pons, S. *Chem. Rev.* **1988**, *88*, 673−695.
(4) Takao, K.; Takao, S.; Scheinost, A. C.; Bernhard, G.; Hennig, C. *Inorg. Chim. Acta* **2010**, *363* (4), 802−806.
(5) Zak, J. K.; Butler, J. E.; Swain, G. M. *Anal. Chem.* **2001**, *73* (5), 908−914.
(6) Rusinek, C. A.; Becker, M. F.; Rechenberg, R.; Kaval, N.; Ojo, K.; Heineman, W. R. *Electroanalysis* **2016**, *28* (9), 2228−2236.
(7) Wächter, N.; Munson, C.; Jarošová, R.; Berkun, I.; Hogan, T.; Rocha-Filho, R. C.; Swain, G. M. *ACS Appl. Mater. Interfaces* **2016**, *8* (42), 28325−28337.
(8) Cobb, S. J.; Ayres, Z. J.; Macpherson, J. V. *Ann. Rev. Anal. Chem.* **2018**, *11*, 463−484.
(9) Vandersande, J. W.; Zoltan, L. D. *Diamond Relat. Mater.* **1995**, *4* (5−6), 641−644.
(10) Tumilty, N.; Welch, J.; Ye, H.; Balmer, R. S.; Wort, C.; Lang, R.; Jackman, R. B. *Appl. Phys. Lett.* **2009**, *94* (5), No. 052107, DOI: 10.1063/1.3075860.
(11) Kim, D. Y.; Yang, J. C.; Kim, H. W.; Swain, G. M. *Electrochim. Acta* **2013**, *94*, 49−56.
(12) Macpherson, J. V. *Phys. Chem. Chem. Phys.* **2015**, *17* (5), 2935−2949.
(13) Macpherson, J. V. *The Use of Conducting Diamond in Electrochemistry*; Alkire, R.; Bartlett, P.; Lipkowski, J., Eds.; John Wiley and Sons Inc., 2015; pp 163−210.
(14) Alfaro, M. A. Q.; Ferro, S.; Martínez-Huitle, C. A.; Vong, Y. M. *J. Braz. Chem. Soc.* **2006**, *17* (2), 227−236.
(15) Mackuľak, T.; Medvecká, E.; Vojs Staňová, A.; Brandeburová, P.; Grabic, R.; Golovko, O.; Marton, M.; Bodík, I.; Medveďová, A.; Gál, M.; Planý, M.; Kromka, A.; Špalková, V.; Škulcová, A.; Horáková, I.; Vojs, M. *Vacuum* **2020**, *171*, No. 108957, DOI: 10.1016/j.vacuum.2019.108957.
(16) Manivannan, A.; Tryk, D. A.; Fujishima, A. *Electrochem. Solid-State Lett.* **1999**, *2* (9), 455−456.
(17) Brycht, M.; Baluchova, S.; Taylor, A.; Mortet, V.; Sedlakova, S.; Klimsa, L.; Kopeček, J.; Schwarzova-Peckova, K. *Bioelectrochemistry* **2021**, *137*, No. 107646.
(18) Zhang, L.; Yang, J.-q.; Luo, Y.; Shang, J.-c.; Jiang, X.-h. Simultaneous determination of eleven compounds related to metabolism of bioamines in rat cortex and hippocampus by HPLC-ECD with boron-doped diamond working electrode. *J. Pharm. Biomed. Anal.***2016**, *118*, 41−51..
(19) Mitani, N.; Einaga, Y. *J. Electroanal. Chem.* **2009**, *626* (1−2), 156−160.
(20) Gupta, S.; Muralikiran, M.; Farmer, J.; Cao, L. R.; Downing, R. G. *J. Mater. Res.* **2009**, *24* (4), 1498−1512.
(21) Maher, C. J.; Bouyer, C.; Griffiths, T. L.; Legand, S.; Leturcq, G.; Miguirditchian, M.; Sarsfield, M. *Radiochim. Acta* **2018**, *106* (2), 95−106.
(22) Ekimov, E. A.; Ralchenko, V.; Popovich, A. *Diamond Relat. Mater.* **2014**, *50*, 15−19.
(23) Kado, Y.; Goto, T.; Hagiwara, R. *Diamond Relat. Mater.* **2009**, *18* (9), 1186−1190.
(24) Goia, S.; Turner, M. A. P.; Woolley, J. M.; Horbury, M. D.; Borrill, A. J.; Tully, J. J.; Cobb, S. J.; Staniforth, M.; Hine, N. D. M.; Burriss, A.; Macpherson, J. V.; Robinson, B. R.; Stavros, V. G. *Chem. Sci.* **2022**, *13* (2), 486−496.
(25) Goia, S.; Richings, G. W.; Turner, M. A.; Woolley, J. M.; Tully, J. J.; Cobb, S. J.; Burriss, A.; Robinson, B. R.; Macpherson, J. V.; Stavros, V. G. *ChemPhotoChem* **2024**, No. e202300325.
(26) Einaga, Y. *Acc. Chem. Res.* **2022**, *55* (24), 3605−3615.
(27) Wood, G. F.; Rodríguez, I. M. T.; Tully, J. J.; Chaudhuri, S.; Macpherson, J. V. *J. Electrochem. Soc.* **2021**, *168* (12), No. 126514.
(28) The Element Six CVD Diamond Handbook (https://e6cvd.com/media/wysiwyg/pdf/E6_CVD_Diamond_Handbook_A5_v10X.pdf).
(29) https://e6cvd.com/us/application/electrochemistry/ep-poly-5-0x9-0mm-0-35mm-thick-np.html.
(30) Cobb, S. J.; Laidlaw, F. H.; West, G.; Wood, G.; Newton, M. E.; Beanland, R.; Macpherson, J. V. *Carbon* **2020**, *167*, 1−10.
(31) Read, T. L.; Macpherson, J. V. *J. Visualized Exp.* **2016**, No. 107, No. e53484.
(32) Ayres, Z. J.; Borrill, A. J.; Newland, J. C.; Newton, M. E.; Macpherson, J. V. *Anal. Chem.* **2016**, *88* (1), 974−980.
(33) Lucio, A. J.; Macpherson, J. V. *Anal. Chem.* **2020**, *92* (24), 16072−16078.
(34) Lucio, A. J.; Meyler, R. E. P.; Edwards, M. A.; Macpherson, J. V. *ACS Sens.* **2020**, *5* (3), 789−797.
(35) Read, T. L.; Cobb, S. J.; Macpherson, J. V. *ACS Sens.* **2019**, *4* (3), 756−763.
(36) Ushizawa, K.; Watanabe, K.; Ando, T.; Sakaguchi, I.; Nishitani-Gamo, M.; Sato, Y.; Kanda, H. *Diamond Relat. Mater.* **1998**, *7* (11−12), 1719−1722.
(37) Mermoux, M.; Marcus, B.; Swain, G. M.; Butler, J. E. *J. Phys. Chem. B* **2002**, *106* (42), 10816−10827.
(38) Mortet, V.; Gregora, I.; Taylor, A.; Lambert, N.; Ashcheulov, P.; Gedeonova, Z.; Hubik, P. *Carbon* **2020**, *168*, 319−327.
(39) Lucchese, M. M.; Stavale, F.; Ferreira, E. M.; Vilani, C.; Moutinho, M. V. D. O.; Capaz, R. B.; Achete, C. A.; Jorio, A. *Carbon* **2010**, *48* (5), 1592−1597.
(40) Khomich, A. A.; Kononenko, V.; Kudryavtsev, O.; Zavedeev, E.; Khomich, A. V. *Nanomaterials* **2023**, *13* (1), 162.
(41) Dychalska, A.; et al. *Mater. Sci.-Pol.* **2015**, *33* (4), 799−805.
(42) Amer, M. S.; et al. *J. Raman Spectrosc.* **1999**, *30* (10), 947−950.
(43) Bard, A.; Faulkner, L.; White, H. *Electrochemical Methods: Fundamentals and Applications*; John Wiley & Sons.
(44) Nicholson, R. S. *Anal. Chem.* **1965**, *37* (11), 1351−1355.
(45) Granger, M. C.; Swain, G. M. *J. Electrochem. Soc.* **1999**, *146*, 4551.
(46) Jarosova, R.; De Sousa Bezerra, P.; Munson, C.; Swain, G. *Phys. Status Solidi A* **2016**, *213* (8), 2087−2098.
(47) Xu, J.; Yokota, Y.; Wong, R. A.; Kim, Y. K.; Einaga, Y. *J. Am. Chem. Soc.* **2020**, *142* (5), 2310−2316.
(48) Sun, J.; Lu, H.; Lin, H.; Du, L.; Huang, W.; Li, H.; Cui, T. *Sep. Purif. Technol.* **2012**, *88*, 116−120.
(49) Poh, W. C.; Log, K. P.; Zhang, W. D.; Sudhiranja; Ye, J.-S.; Sheu, F.-S. *Langmuir* **2004**, *20* (13), 5484−5492.
(50) Trouillion, R.; O'Hare, D.; Einaga, Y. *Phys. Chem. Chem. Phys.* **2011**, *13*, 5422−5429.
(51) Brycht, M.; Baluchova, S.; Taylor, A.; Mortet, V.; Sedlakova, S.; Klimsa, L.; Kopecek, J.; Schwarzova-Peckova, K. *Bioelectrochemistry* **2021**, *137*, No. 107646.
(52) Liu, D.-Q.; Chen, C.-H.; Perry, D.; West, G.; Cobb, S. J.; Macpherson, J. V.; Unwin, P. R. *ChemElectroChem* **2018**, *5* (20), 3028−3035.
(53) Bennett, J. A.; Wang, J.; Show, Y.; Swain, G. M. *J. Electrochem. Soc.* **2004**, *151*, No. E306.
(54) Martin, H. B.; Argoitia, A.; Landau, U.; Anderson, A. B.; Angus, J. C. *J. Electrochem. Soc.* **1996**, *143*, L133.
(55) Granger, M. C.; Witek, M.; Xu, J.; Wang, J.; Hupert, M.; Hanks, A.; Koppang, M. D.; Butler, J. E.; Lucazeau, G.; Mermoux, M.; Strojek, J. W.; Wain, G. M. *Anal. Chem.* **2000**, *72* (16), 3793−3804.
(56) McCreery, R. L. *Chem. Rev.* **2008**, *108* (7), 2646−2687.
(57) *Laboratory Techniques in Electroanalytical Chemistry, Revised and Expanded*; Kissinger, P.; Heineman, W. R., Eds.; CRC press, 2018.
(58) Dai, Y.; Proshlyakov, D.; Zak, J.; Swain, G. *Anal. Chem.* **2007**, *79* (19), 7526−7533.
(59) Petek, M.; Neal, T.; Murray, R. *Anal. Chem.* **1971**, *43* (8), 1069−1074.

NOTE ADDED AFTER ASAP PUBLICATION

This paper was published ASAP on November 13, 2024 with an error in Figure 6. The figure was replaced and the revised manuscript was reposted on November 13, 2024.